



HAL
open science

Analysis of shock-wave diffraction over double cylindrical wedges. Part II: Vorticity generation

N. Brahmi, A. Hadjadj, V. Soni, A. Chaudhuri

► To cite this version:

N. Brahmi, A. Hadjadj, V. Soni, A. Chaudhuri. Analysis of shock-wave diffraction over double cylindrical wedges. Part II: Vorticity generation. *Acta Astronautica*, 2020, 172, pp.140 - 150. 10.1016/j.actaastro.2020.02.017 . hal-03490299

HAL Id: hal-03490299

<https://hal.science/hal-03490299>

Submitted on 20 May 2022

HAL is a multi-disciplinary open access archive for the deposit and dissemination of scientific research documents, whether they are published or not. The documents may come from teaching and research institutions in France or abroad, or from public or private research centers.

L'archive ouverte pluridisciplinaire **HAL**, est destinée au dépôt et à la diffusion de documents scientifiques de niveau recherche, publiés ou non, émanant des établissements d'enseignement et de recherche français ou étrangers, des laboratoires publics ou privés.



Distributed under a Creative Commons Attribution - NonCommercial 4.0 International License

1 Analysis of shock-wave diffraction over double cylindrical
2 wedges. Part II: Vorticity Generation

3 N. Brahmi^{a,*}, A. Hadjadj^a, V. Soni^a, A. Chaudhuri^b

4 ^a*Normandie University, INSA of Rouen, CNRS, CORIA, 76000 Rouen, France*

5 ^b*Department of Civil Engineering and Energy Technology, OsloMet – Oslo Metropolitan*
6 *University, Pilestredet 35, PB 4, St. Olavs Plass, 0130, Oslo, Norway*

7 **Abstract**

The unsteady aspect of turbulent flow structures generated by a shock-wave diffraction over double cylindrical wedges, with initial diffracting angle of 75° , are numerically investigated by means of two-dimensional high-fidelity numerical simulation. Different incident-shock-Mach numbers, ranging from transonic to supersonic regimes, are considered. Unlike previous studies where only the total vorticity production is evaluated, the current paper offers more insights into the spatio-temporal behavior of the circulation by evaluating the evolution of the instantaneous vorticity equation balance. The results show, for the first time, that the diffusion of the vorticity due to the viscous effects is quite important compared to the baroclinic term for low Mach numbers regimes, while this trends is inverted for higher Mach numbers regimes. It is also found that the stretching of the vorticity due to the compressibility effects plays an important role in the vorticity production. In terms of pressure impulses, the effect of the first concave surface on the shock strength has been quantified at both earlier and final stages of the shock diffraction process. Unlike the overpressure, the static and the dynamic pressure impulses are shown to be significantly reduced at the end of the first concave surface.

8 *Keywords:* Shock wave, Shock diffraction, Vorticity, Vorticity transport,
9 Numerical simulation

*Corresponding author

Email address: nassim.brahmi@insa-rouen.fr (N. Brahmi)

10 Nomenclature

E	total energy per unit mass
e	internal energy per unit mass
I_p	static-pressure impulse
I_{pd}	dynamic-pressure impulse
M_s	incident-shock-Mach number
\mathcal{P}	normalized overpressure
Pr	Prandtl number
p	static pressure
\mathcal{R}	universal gas constant
R	concave radius
T	temperature
t	time
\mathbf{v}	velocity vector

Greeks

Γ	vorticity circulation
γ	heat capacity ratio
λ	thermal conductivity
μ	dynamic viscosity
ρ	density
ω	local vorticity
ω_1	angle of the first wedge
ω_2	angle of the second wedge
ω_c	convection vorticity term
ω_t	unsteady vorticity term

Abbreviations

BAR	baroclinic torque
DFV	diffusion of vorticity due to viscosity
IBM	immersed-boundary method
I	incident shock wave

LS	lambda shock
PV	primary vortex
r	reflected shock wave
SLI	shear-layer instabilities
SS	secondary shocks
SV	secondary vortex
VSC	stretching of vorticity due to compressibility
VSG	stretching/tilting of vorticity due to velocity gradients
VTE	vorticity transport equation
WENO	weighted essentially non-oscillatory

11 1. Introduction

12 The unsteady evolution of vortex rings produced by a shock diffraction un-
13 dergoing a sudden expansion area is one of the most fascinating phenomenon
14 in high-speed flows. This process was observed many decades ago [1], [2], [3],
15 with different levels of qualitative description [4] and numerical modelling [5],
16 [6], [7]. For instance, Skews [1] have discussed the behavior of disturbances
17 produced in the perturbed region caused by the passage of a shock wave, whose
18 Mach number varies from 1.0 to 5.0, through a convex corner. The experimental
19 results of this study have shown that the velocities of the contact surface and
20 the secondary shock become independent of the corner angles greater than 75° .
21 Sun and Takayama [5] have evaluated numerically the vorticity production in
22 a shock-wave diffraction problem over convex corners, with angles varied from
23 5° to 180° . The authors proposed an analytical model to evaluate the total
24 vorticity production generated by the slipstream. They found that the rate of
25 vorticity production is always increasing with the corner angle and the shock
26 strength. They also reported that the slipstream is at the origin of the total
27 vorticity generation and it can be the more dominating factor in producing vor-
28 ticity in compressible flows in comparison to baroclinic effects. In another study,
29 Sun and Takayama [8] have investigated the formation of secondary shock waves

30 behind the incident shock wave. Accordingly, the threshold shock-wave Mach
31 number was found to be $M_s = 1.346$ for a gas with $\gamma = 1.4$, when neglecting
32 viscous effects on the formation of this secondary shock waves.

33 Quinn and Kontis [9] have investigated a shock-wave diffraction around a
34 172° corner at $M_s = 1.46$ using both numerical simulations and experimental
35 visualizations. Their numerical study showed that although the evolution of
36 the shear layer was obtained for very fine mesh, some very fine flow structures
37 were under predicted. Cai *et al.* [10] have investigated the effect of back-
38 pressure on the shock train location and its structure in a straight isolator. It is
39 shown that the structure of the shock train largely depends on the relative Mach
40 number and is very sensitive to it. Concerning the average back-pressure, it has
41 a great influence on the location of the shock train in the oscillating region,
42 while its amplitude has a noticeable effect on the size of this oscillating region.
43 Reeves and Skews [11] have investigated both numerically and experimentally
44 the unsteady aspects of three-dimensional shock-wave diffraction phenomena.
45 They found that the trends of circulation production correlated quite well with
46 those obtained from the two-dimensional diffraction case. Furthermore, they
47 showed that the rate of vorticity production tends to be constant once the
48 incident shock wave had fully diffracted over the surface edge. Finally, the
49 shape of the diffracting edge appeared to have no significant impact on the
50 results.

51 Abate and Shyy [12] studied the dynamics of shock-wave diffraction using the
52 vorticity transport equation. They discussed the link between high-strain rates
53 resulting from the expansion corner to the solenoidal dissipation rates and the
54 stress rates to the dilatational dissipation rates of turbulent kinetic energies. The
55 baroclinic torque enhances the vorticity generation in such interaction. Their
56 study indicates that both viscous effects and small-scale turbulent dissipation
57 are important for the evolution of the primary vortex as well as the small vortices
58 generated by the Kelvin-Helmholtz instability. Zhao *et al.* [13] have investigated
59 the shock wave focusing process with shock-turbulence interaction in a parabolic
60 cavity with various intensity of shock and vortex strength. Their numerical

61 results show that the net dilatational vorticity is the most dominant part in
62 vorticity transport, followed by the baroclinic vorticity and the viscous vorticity
63 generation.

64 Gnani *et al.* [4] have used experimental schlieren photography to qualita-
65 tively evaluate the development of a shock-wave diffraction around sharp and
66 curved splitters. Recently, Chaudhuri and Jacobs [7] performed numerical anal-
67 ysis of shock-wave diffraction over a sharp splitter plate. The objective was to
68 address a detailed analysis of the flow evolution using the probability density
69 functions of various enstrophy equation parameters as well as the invariants of
70 the velocity gradient tensor. Their study reveals the mechanism of unwinding
71 of vortices and its link with the divergence of the Lamb vector.

72 Additionally, Tseng and Yang [6] investigated numerically shock-wave
73 diffraction around a convex corner by solving both Euler and Navier-Stokes
74 equations. The vorticity production formed during the shock-wave diffraction
75 and the subsequent interaction between the reflected shock and the main vortex
76 core have been analyzed. Different circulation production rates are observed
77 between Euler and Navier-Stokes solutions as a result of the vorticity contribu-
78 tion from the boundary layer and the secondary vortex. It was also found that
79 the reflection influences the rate of vorticity production, which is found to be
80 dependent on the strength of the incident shock wave and the diffracting angle.

81 Chaudhuri *et al.* [14] used an immersed boundary (IB) method to study
82 the interaction of the moving shock through an array of cylinder matrix. Their
83 analysis confirmed earlier findings of Sun and Takayama [5], where the baroclinic
84 production of the vorticity is found to be feeble. Recently, Soni *et al.* [15] have
85 conducted numerical investigations of shock-wave reflection over double-concave
86 cylindrical reflectors, where new shock reflection topologies were found.

87 The aim of the present study is to further analyze the evolution of the
88 instantaneous vorticity production and the flow structure in shock diffraction
89 problem.

90 2. Governing equations and numerics

91 The compressible Navier-Stokes equations for an ideal gas are given by:

$$\partial_t \rho + \operatorname{div}(\rho \mathbf{v}) = 0 \quad (1)$$

$$92 \quad \partial_t(\rho \mathbf{v}) + \operatorname{div}(\rho \mathbf{v} \otimes \mathbf{v}) + \nabla p = \nabla \tau \quad (2)$$

$$93 \quad \partial_t(\rho E) + \operatorname{div}(\rho E \mathbf{v}) + \operatorname{div}(\rho \mathbf{v}) = \nabla(\tau \mathbf{v} + \lambda \nabla T) \quad (3)$$

$$94 \quad p = (\gamma - 1)\rho e, \quad E = \frac{1}{2}|\mathbf{v}|^2 + e \quad (4)$$

$$95 \quad \tau = \mu \left[\nabla \otimes \mathbf{v} + (\nabla \otimes \mathbf{v})^T - \frac{2}{3}(\nabla \cdot \mathbf{v})\mathbf{I} \right] \quad (5)$$

96 where t stands for the time, ρ , \mathbf{v} , p , E , T , λ , μ , e are the density, velocity
97 vector, pressure, total energy per unit mass, temperature, thermal conductivity,
98 dynamic viscosity and internal energy, respectively. The working gas is air with
99 $\gamma = 1.4$ and Prandtl number $Pr = 0.72$. The fluid viscosity follows Sutherland's
100 law.

101 To simulate the flow field, we used an *in-house* compressible parallel solver
102 equipped with adaptive multi-resolution method [16, 17] for mesh refinement.
103 The code uses an immersed-boundary method (IBM) to handle fluid-solid inter-
104 action problems [18, 14]. The solid body is embedded into a Cartesian grid and
105 tracked using a ray-tracing technique. Inviscid and viscous fluxes are computed
106 using a fifth-order weighted essentially non-oscillatory (WENO 5) scheme and a
107 fourth-order central difference formula, respectively, while the time is advanced
108 using a third-order Runge-Kutta method [19].

109 3. Problem set-up

110 As in Brahmi *et al.* [20], a two-dimensional problem of shock diffraction over
111 double concave geometry, with constant radius of $R = 50 \text{ mm}$ and wedge angles
112 $\omega_1 = \omega_2 = 75^\circ$, is considered. As for the computational specifications, the
113 boundary conditions were set to inlet and outlet at the left and the right sides

114 of the computational domain, respectively, while the top and the bottom-right
 115 boundaries are considered as symmetry planes. On the solid surface, no-slip
 116 boundary conditions are applied. The incident-shock-Mach number was varied
 117 from 1.6 to 4.5. For all those Mach numbers, the shock is initially located 5
 118 mm ahead of the first concave surface corner. Rankine-Hugoniot relations are
 119 used to fix the initial conditions for both left (shocked gas) and right (stagnant
 120 flow) states at a given M_s . Air is considered as a working fluid and the initial
 121 stagnant flow is assigned with temperature $T_0 = 300 K$ and pressure $p_0 = 101.3$
 122 kPa. Given the sensitivity of the phenomena to the grid resolution, a grid
 123 dependency study is conducted in order to determine the grid resolution effect
 124 on the results. Five different meshes were used for $M_s = 1.6$, as summarized in
 Table 2.

Grid	$\Delta x_{min} (\mu m)$	$\Delta y_{min} (\mu m)$	number of points (MP)
\mathcal{G}_0	95	88	1.83
\mathcal{G}_1	60	50	5.04
\mathcal{G}_2	40	40	8.84
\mathcal{G}_3	30	29	17.3
\mathcal{G}_4	20	21	33.55

Table 2: Different grid resolutions used for a given incident shock-wave Mach number of $M_s = 1.6$ (MP: million points).

125

126 4. Results and discussion

127 Figures 1(a) and 1(b) show the flow structures behind the diffracting shock
 128 wave for the first and the second concave surfaces, respectively. Shortly after
 129 the penetration of the shock into the cavity, the expanding flow evolves into a
 130 complicated system of distorted and secondary shocks with separated regions
 131 and vortices formation. As shown in Figure 1, an end-wall corner vortex (PV) is
 132 formed at $M_s = 1.6$ with a rolling-up of eddies that are convected away from the
 133 concave entrance as the diffraction process evolves. In addition to this important
 134 primary vortex, a secondary instability (SV) appears along the surface wall. The
 135 Reynolds number, based on the shocked flow properties (density, speed of sound,

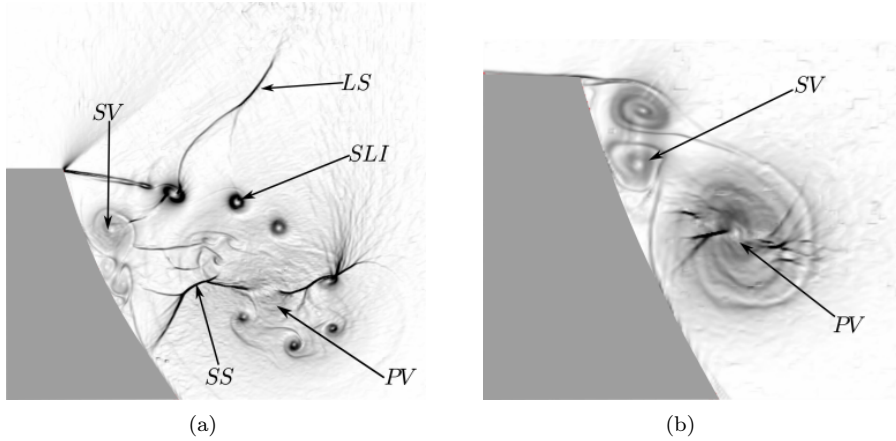


Figure 1: Numerical schlieren pictures for $M_s = 1.6$ (a): first concave at $t = 184 \mu s$ (b): second concave at $t = 292 \mu s$. PV: Primary vortex, SV: Secondary vortex, LS: Lambda shock, SLI: Shear layer instabilities, SS: secondary shock (shocklets).

136 viscosity in the upstream of the shock and the radius of curvature R), is of the
 137 order of 10^6 .

138 4.1. Vorticity production

139 In order to investigate the dynamics of the shear-layer formation, the vor-
 140 ticity production is first analyzed in term of total recirculation Γ as:

$$\Gamma = \int_s \omega ds = \int_L u dl \quad (6)$$

141 where the integral contour (path L) is taken along the boundary so that to
 142 enclose the perturbed region behind the shock wave. The integral contour is
 143 depicted in Figure 2 by a dashed red line. For better characterization of the
 144 vorticity production in shock-wave diffraction, the ratio of circulation to time,
 145 Γ/t , is used. The rate of circulation production is related to the incident shock-
 146 Mach number M_s , the diffraction angle and the gas properties. For a given gas
 147 and diffraction angle, the ratio Γ/t can be uniquely determined as a function of
 148 M_s [5] as:

$$\frac{\Gamma}{t} = f(M_s) \quad (7)$$

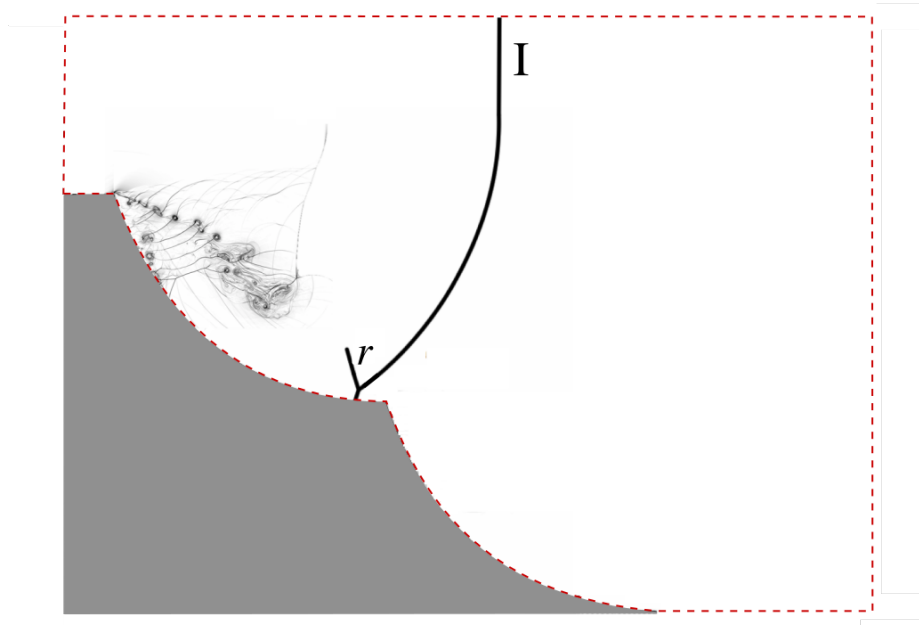


Figure 2: Schematic representation of double concave surfaces, $---$ integral path L , I : incident shock wave, r : reflected shock wave.

149 In this paper, the calculation of the circulation is directly obtained from the
 150 summation of the vorticity over each individual surface area. In general, the
 151 calculation of the circulation is performed only in the perturbed region behind
 152 the shock. However, in this study the total amount of circulation is calculated
 153 over the entire computational domain since the unperturbed flow regions (uni-
 154 form flow) provides almost no contribution to the circulation.

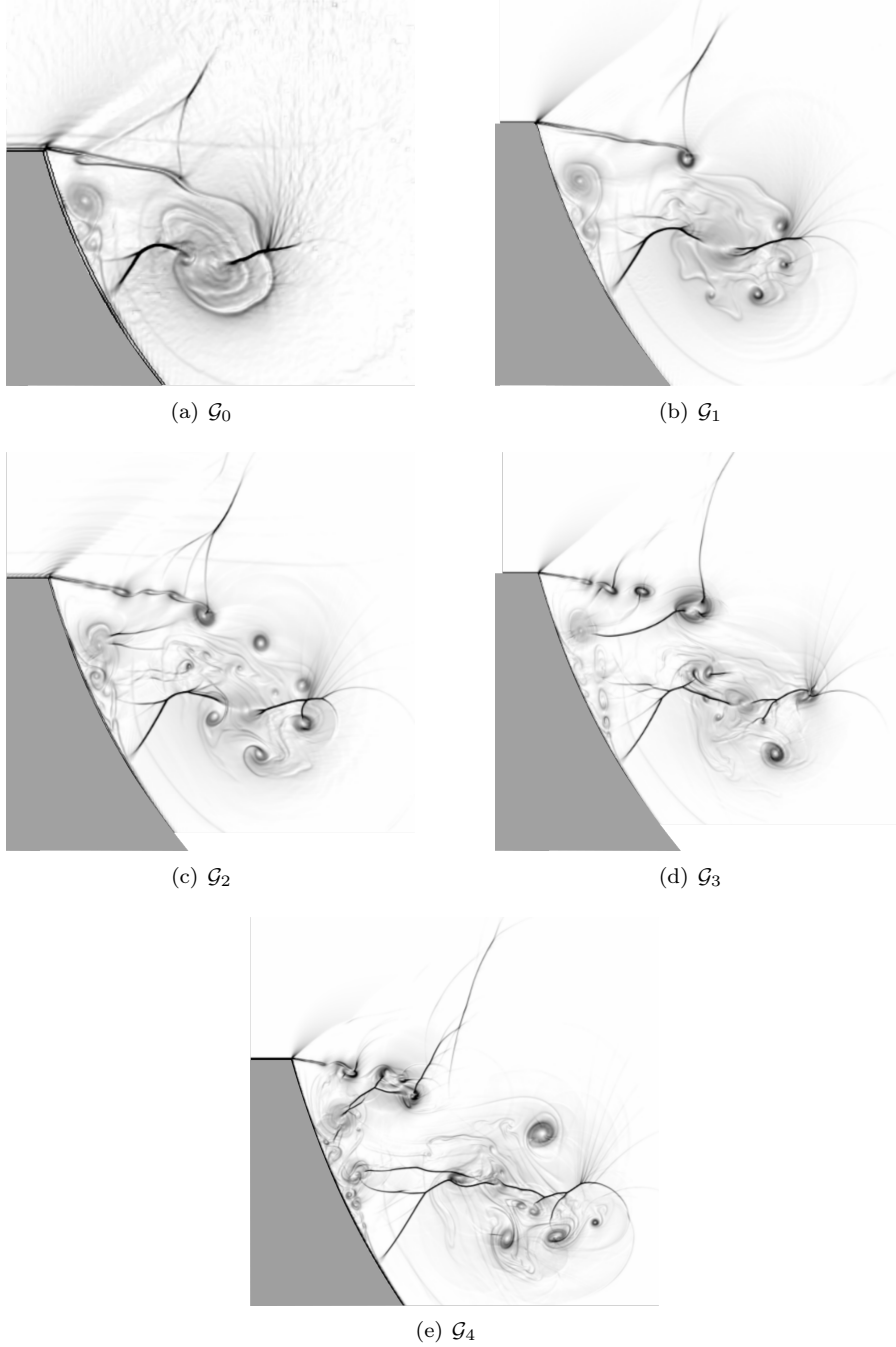


Figure 3: Numerical schlieren pictures for different grid resolutions at $t = 150 \mu s$ with $M_s = 1.6$.

155 As it can be seen in Figure 3, the flow topology of the primary vortex changes
 156 with the mesh resolution, the global variation of the vorticity production (Γ)
 157 and its rate (Γ/t) are insensitive to the grid resolution (see Figures 4(a) and
 158 4(b)). Indeed, the circulation Γ increases linearly in time regardless of the grid
 159 resolution. The results for the rate of vorticity production (Γ/t) are scaled by the
 160 product $\mathcal{R} \times T_0$, where \mathcal{R} is the universal gas constant divided by the molecular
 161 weight of air taken as, $\mathcal{R} = 287 \text{ J.Kg}^{-1}.\text{K}^{-1}$ and T_0 is the temperature in
 162 front of the incident shock ($T_0 = 300 \text{ K}$). Since the rate has the dimension
 163 of the square of the velocity (m^2s^{-2}), one may obtain dimensional results by
 164 multiplying the dimensionless values by $\mathcal{R} \times T_0$,

$$\frac{\Gamma'}{t'} = \mathcal{R} \times T_0 \frac{\Gamma}{t} \quad (8)$$

165 Note that all the results of the rate of vorticity production, Γ/t , presented in
 166 this paper are dimensionless values.

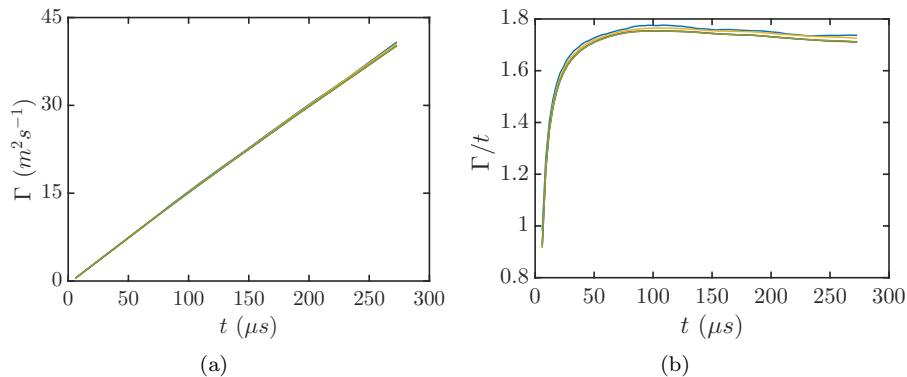


Figure 4: Time history of (a): circulation (b): rate of circulation production for $M_s = 1.6$ and different mesh resolutions (\mathcal{G}_0 , \mathcal{G}_1 , \mathcal{G}_2 , \mathcal{G}_3 , \mathcal{G}_4).

167 The effect of shock strength on the vorticity production is investigated by
 168 changing M_s using the grid \mathcal{G}_4 . The results are shown in Figures 5(a) and 5(b).
 169 Basically both quantities increase with M_s . In other words, the strength of
 170 the main vortex increases at higher values of Mach number, and increase much
 171 faster for stronger shock waves as reported by Sun and Takayama [5]. The
 172 vorticity production occurs before the diffraction of the incident shock wave (at
 173 $t = 12 \mu s$ for $M_s = 2.0$) as a result of the boundary-layer formation on the
 174 solid wall. This demonstrates the role played by viscous effects in forming the
 175 shock-wave diffraction structure as mentioned by Tseng and Yang [6]. Figure
 176 5(b) shows the rate of the circulation production. The five curves reach different
 177 constant values of 1.78, 3.79, 5.72, 11.42 and 18.73 for $M_s = 1.6, 2.0, 2.5, 3.5$ and
 178 4.5, respectively. Similar trends were observed by Sun and Takayama [5] with
 179 constant values known as invariants of Euler equations in shock-wave diffraction.
 180

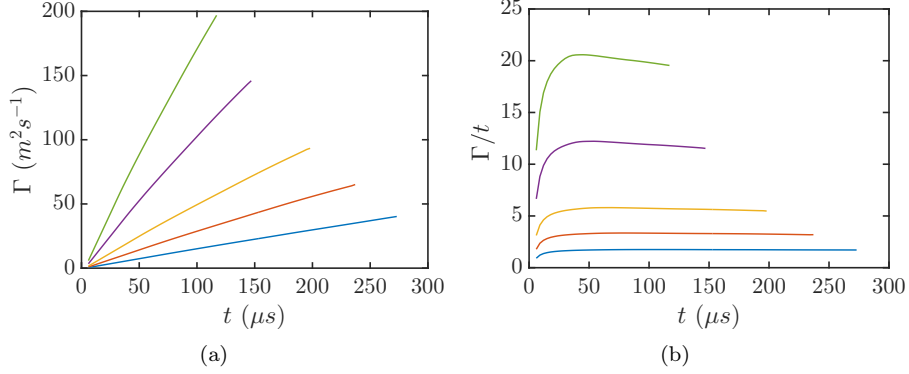


Figure 5: Time history of (a): circulation (b): rate of circulation production for different incident-shock-Mach numbers ($- M_s = 1.6$, $- M_s = 2.0$, $- M_s = 2.5$, $- M_s = 3.5$, $- M_s = 4.5$).

181 Figure 6 represents vorticity maps at different instants ($t = 48 \mu\text{s}$, $78 \mu\text{s}$
 182 and $108 \mu\text{s}$) for $M_s = 2.0$. As it can be seen, the main vortex and the highly
 183 disturbed shear layer split when interacting with the secondary shock waves.
 184 This results in a generation of fine scale turbulent eddies. Note that the pro-
 185 duction of vorticity is mainly concentrated in this turbulent region compared to
 186 the compression zone.

187 4.2. Vorticity transport equation

188 The vorticity transport equation provides further details on the mechanism
 189 of the vortex dynamics, it can be written as follows:

$$\frac{D\omega}{Dt} = \underbrace{(\omega \cdot \nabla)u}_{\text{VSG}} - \underbrace{\omega(\nabla \cdot u)}_{\text{VSC}} + \underbrace{\frac{1}{\rho^2}(\nabla\rho \times \nabla p)}_{\text{BAR}} + \underbrace{\nabla \times \left(\frac{\nabla \cdot \tau}{\rho}\right)}_{\text{DFV}} \quad (9)$$

190 where the left-hand side represents the material derivative expressed as the
 191 sum of unsteady, ω_t , and convection, ω_c , terms. Here, $\omega_t = \partial\omega/\partial t$ and $\omega_c =$
 192 $U(\partial\omega/\partial x) + V(\partial\omega/\partial y)$.

193 The first term in the right-hand side of Eq. (9) represents the stretching
 194 or tilting of vorticity due to the flow velocity gradients, a term that is null in
 195 two-dimensional cases. The second term expresses the stretching of vorticity

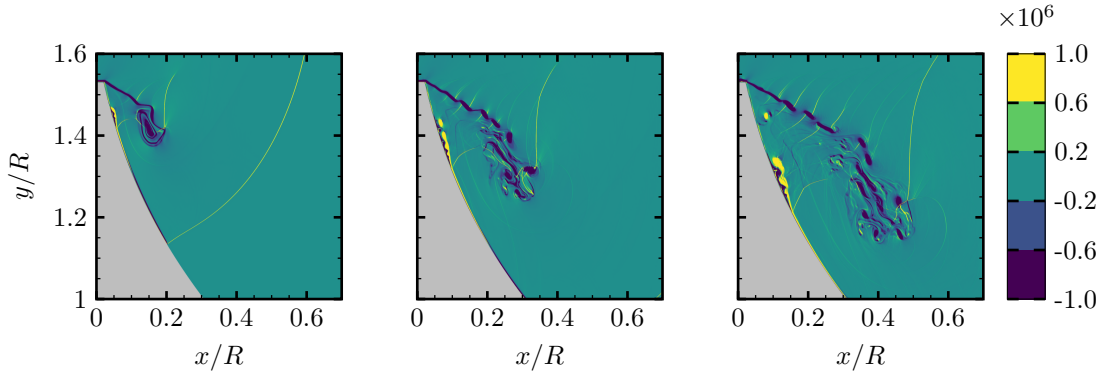


Figure 6: Vorticity maps for $M_s = 2.0$. Column-wise (left-to-right): $t = 48 \mu s$, $78 \mu s$ and $108 \mu s$.

196 due to flow compressibility. The third contribution represents the baroclinic
 197 term, which accounts for the changes in the vorticity due to the intersection of
 198 density and pressure surfaces. The last term represents the diffusion of vorticity
 199 due to the viscous effects.

200 The different expressions appearing in the right-hand side of Eq. (9) are
 201 shown in Figure 7 (in Row-wise) at different time intervals for $M_s = 2.0$. As
 202 one can see, the stretching of the vorticity due to flow compressibility (VSC)
 203 has the most dominant contribution. Based on the VSC contour, it is clear
 204 that there exist locally stretched structures in the core region of the vortex due
 205 to compressibility effect arising from local regions of compression/expansion.
 206 Additionally the results show the existence of evolving large scale vortices which
 207 interact with the different shock patterns present in the flow and finally split
 208 into small-scale vortices.

209 Figure 8 shows the temporal evolution of the vorticity transport equation
 210 (VTE) terms. The stretching of vorticity due to flow compressibility (VSC) is
 211 almost constant over time independently of M_s , while its magnitude increases
 212 with Mach number. This contribution represents the effects of expansion on the
 213 vorticity field and plays a major role in the vorticity dynamics. The baroclinic
 214 term (BAR) is responsible of the generation of vorticity from unequal accel-

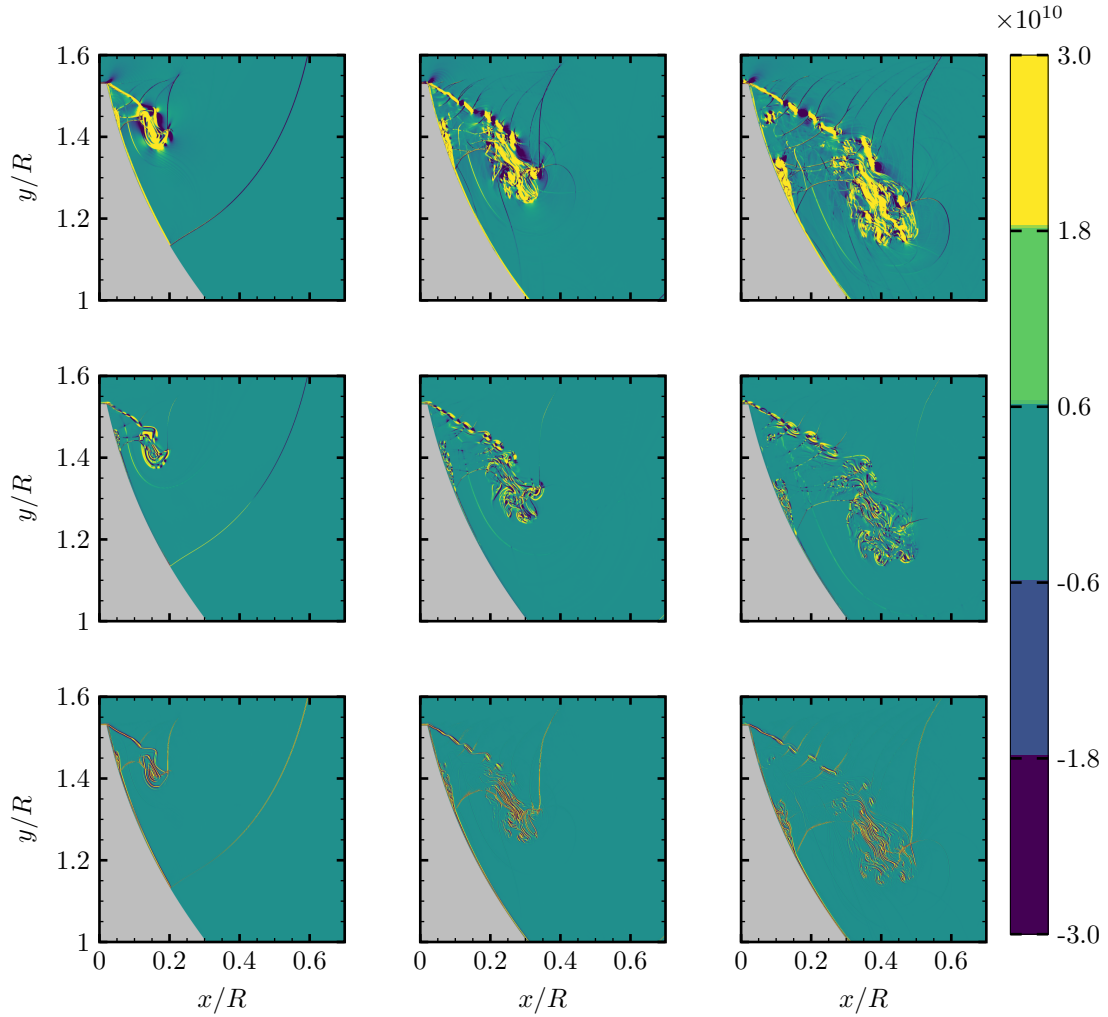


Figure 7: Color maps of vorticity terms for $M_s = 2.0$. Row-wise (top-to-bottom): stretching of the vorticity due to flow compressibility (VSC), baroclinic (BAR) and diffusion of vorticity due to the viscous effects (DFV) terms. Column-wise (left-to-right): $t = 48 \mu s, 78 \mu s$ and $108 \mu s$.

215 eration as a result of nonaligned density and pressure gradients. The lighter
216 density fluid is faster accelerated than the high density one, which result in a
217 shear-layer formation, that contributes to the generation of vorticity. The dif-
218 fusion of vorticity due to the viscous effects (DFV) is essentially enhancing the
219 viscous diffusion process on the vorticity distribution. As a result of viscosity,
220 the vorticity tends to spread out spatially. Note that the diffusion of vorticity
221 due to viscous effects (DFV) is quite important compared to the baroclinic term
222 (BAR) for $M_s \leq 2.5$, while this trends is inverted for $M_s \geq 3.5$. As for the VSC
223 term, the unsteady term, ω_t , which describes the rate of change in vorticity due
224 to flow unsteadiness, is found to be constant in time regardless of M_s . For the
225 convection term, ω_c , we also notice that it is almost constant in time for all
226 shock-wave Mach numbers, and its magnitude increases at higher values of M_s .
227 This term represents the change of vorticity of the moving fluid particles due to
228 the motion of the fluid particle as it moves from one point to another. Figure
229 9 represents contours plots of ω_c for $M_s = 2.0$ at different instants. As we can
230 see, this term is mainly concentrated in the turbulent region as well as in the
231 shear layer and in the near wall-region.

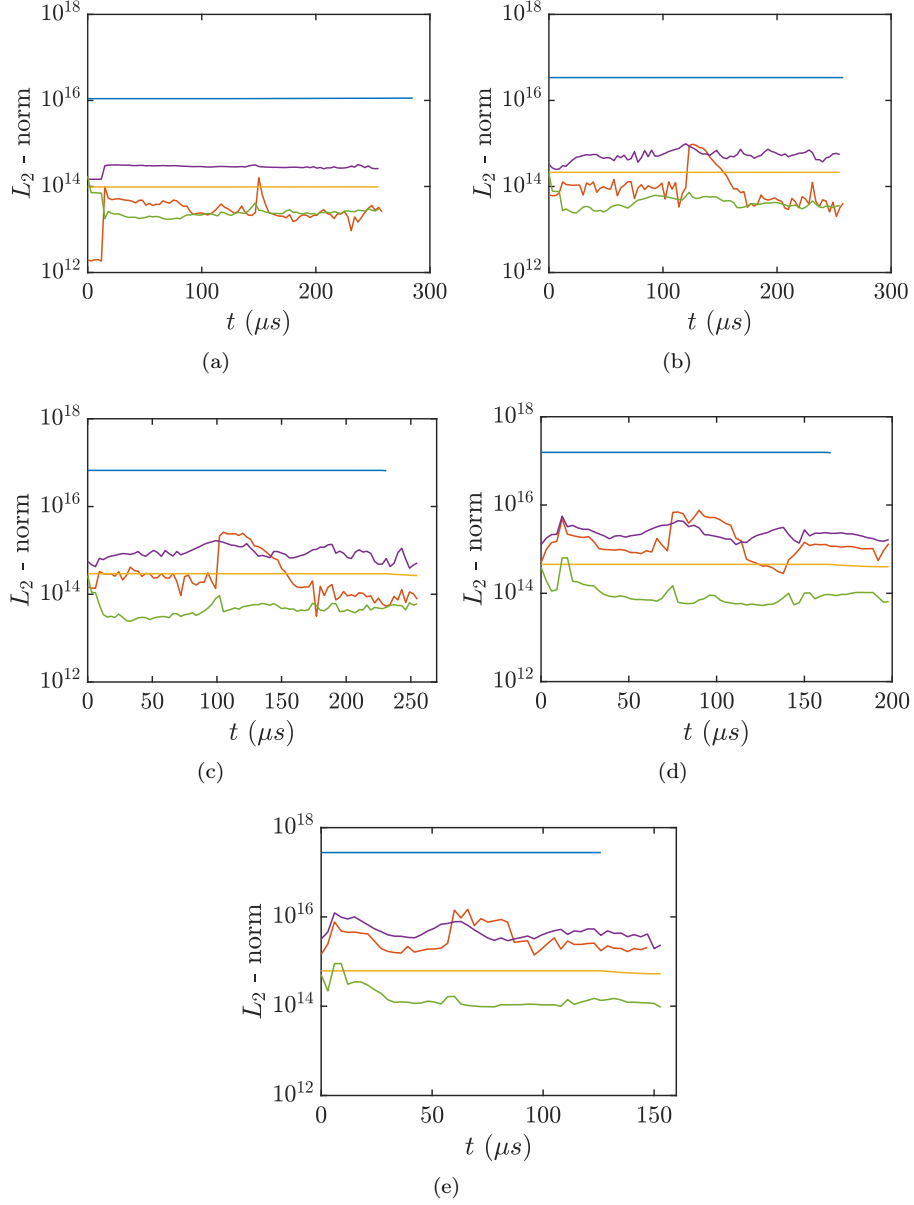


Figure 8: Time history of **normalized vorticity transport equation terms** for (a): $M_s = 1.6$; (b): $M_s = 2.0$; (c): $M_s = 2.5$; (d): $M_s = 3.5$ and (e): $M_s = 4.5$ (—: stretching of the vorticity due to flow compressibility (VSC) term, —: baroclinic (BAR) term, —: diffusion of vorticity due to the viscous effects (DFV) term, —: convection term (ω_c), —: unsteady term (ω_t)).

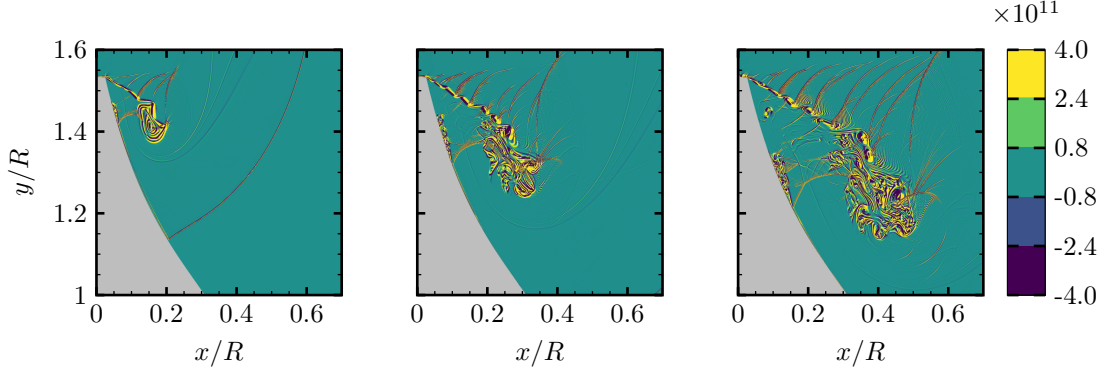


Figure 9: Color maps showing the convection term of vorticity (ω_c) for $M_s = 2.0$. Column-wise (left-to-right): $t = 48 \mu s, 78 \mu s$ and $108 \mu s$.

232 4.3. Static and dynamic pressure impulses and normalized overpressure

233 The effect of M_s on shock strength was investigated by computing the static
 234 and the dynamic pressure impulses along with the normalized overpressure, all
 235 defined as:

$$I_p = \int_{t_0}^{t_f} p dt \quad (10)$$

$$I_{pd} = \int_{t_0}^{t_f} \frac{1}{2} \rho \mathbf{v}^2 dt \quad (11)$$

$$\mathcal{P} = (p - p_0)/p_0 \quad (12)$$

238 where p_0 is the static pressure of gas at rest, p , ρ and \mathbf{v} are the local static
 239 pressure, density and velocity vector in the shocked region (t_0 and t_f being the
 240 initial and the final times). These quantities are calculated at two different
 241 space locations as shown in Figure 10, with $P_1(x_1^*, y_1^*)$ corresponding to the
 242 beginning of the first concave surface, $x_1^* = x_1/R = 0.26$ and $y_1^* = y_1/R = 1.6$
 243 and $P_2(x_2^*, y_2^*)$ corresponding to the beginning of the second concave surface,
 244 $x_2^* = x_2/R = 1.22$ and $y_2^* = y_2/R = 0.86$. The results are presented in Figures
 245 11 and 12, for P_1 and P_2 , respectively.

246 At the upstream location, P_1 , both static and dynamic pressure impulses
 247 are linearly increasing with time for all M_s . The passage of the incident wave
 248 is characterized by a sudden jump in these last two quantities (more visible
 249 for $M_s = 4.5$ as seen in Figures 11(a), 11(b)). This linear increase is due to
 250 the fact that P_1 is located at the inlet where no perturbation exists behind the
 251 shock wave. Concerning the normalized overpressure, one can see in Figure
 252 11(c) a sudden jump caused by the passage of the incident shock. Afterwards,
 253 it remains constant, except for $M_s = 1.6$, where it starts to decrease gradually
 254 as the shock propagates over the double concave surfaces.

255 At the downstream location, P_2 , the flow behavior is completely different.
 256 The static pressure impulse is suddenly increased due to the passage of the
 257 shock. At this early stage of the diffraction process, the increasing rate is
 258 important. However, after the shock wave leads off the end of the geometry,
 259 it decreases giving almost constant value (see Figure 12(a)). For the dynamic
 260 pressure impulse, we observe a sudden increase induced by the passage of the
 261 shock, after this it remains constant for a certain elapsed time until the arrival
 262 of the reflected shock and formation of the shocklets which generate a second
 263 increase due to the gas acceleration. Note that this behavior is more visible for
 264 $M_s = 4.5$ and $M_s = 3.5$ (see Figure 12(b)). **The arrival of the incident shock**
 265 **wave causes a sudden increase of the normalized overpressure (Figure 12(c)).**
 266 **Afterwards, it remains almost constant until the reflected wave (r in Figure**
 267 **10(b)) arrives and causes a second increase. Once the reflected shock passed,**
 268 **the expanded gas gets driven away and causes a strong decrease.** At the last
 269 stage of the diffraction, we can see a succession of peaks due to the passage of
 270 the shocklets and the emergence of flow instabilities in this zone. These peaks
 271 are visible only for high Mach numbers ($M_s = 4.5$, $M_s = 3.5$), for which the
 272 turbulent region is highly perturbed. It is worth noticing that for high M_s the
 273 flow relaxes until it reaches negative overpressure values, because of the strong
 274 vortex suction acting on this highly perturbed turbulent zone.

275 In order to investigate the effect of the first concave surface on the shock
 276 strength, the deficit of various parameters mentioned above is calculated. This

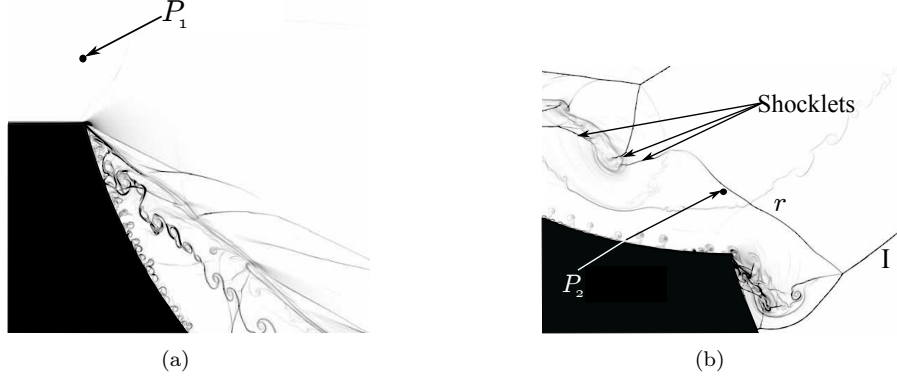


Figure 10: Numerical schlieren pictures for $M_s = 4.5$ at $t = 69 \mu s$: (a) beginning of the first concave surface; (b) beginning of the second concave surface; I: incident shock wave; r : reflected shock wave, P_1 and P_2 are two probes locations.

277 deficit is defined as the ratio of the impulses and overpressure calculated at the
 278 two points: $I_p(P_2)/I_p(P_1)$, $I_{pd}(P_2)/I_{pd}(P_1)$, $\mathcal{P}(P_2)/\mathcal{P}(P_1)$. For static pressure
 279 impulse, we can see that the deficit is more important for the high Mach num-
 280 bers because of the highly turbulent region generated behind the strong shock
 281 wave and the intense vortex suction exerted on the flow (see Figure 13(a)).
 282 By comparing the static and dynamic pressure impulses deficit (Figures 13(a),
 283 13(b), respectively) we can see that the deficit in dynamic pressure impulse is
 284 more important because of the decrease of density and the square of velocity
 285 together. For the overpressure deficit (Figure 13(c)), the peaks are exceeding
 286 unit, which means that the overpressure in P_2 is greater than in P_1 and this is
 287 mainly caused by the passage of the reflected shock which induces the formation
 288 of shocklets (small shocks embedded into turbulent region).

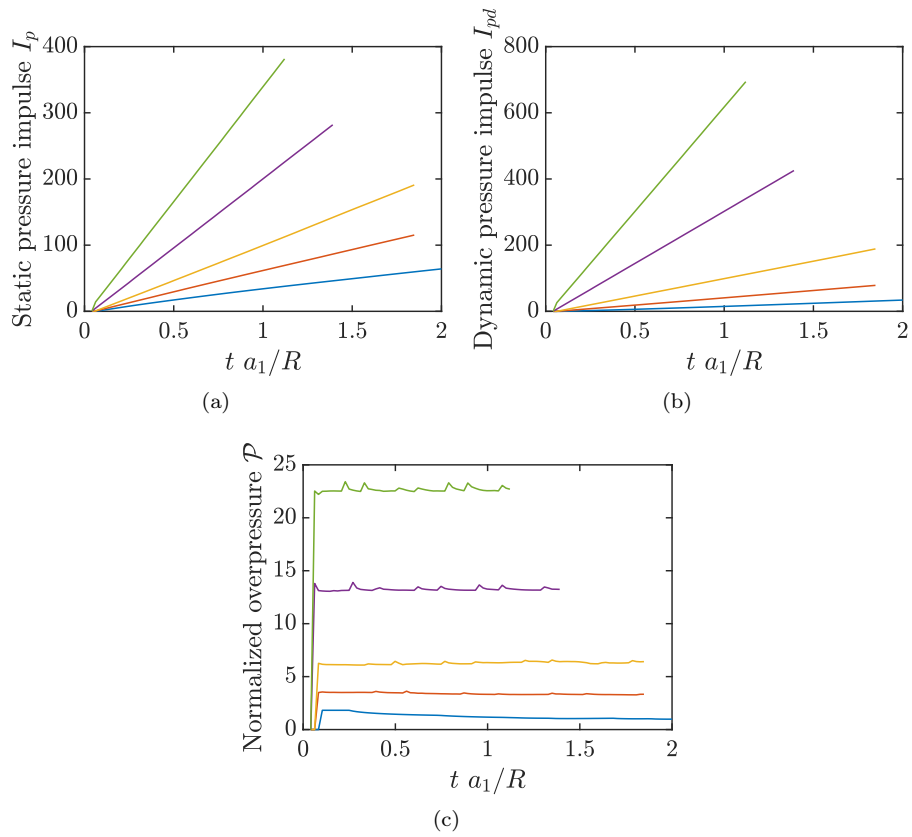


Figure 11: Time history of (a): static pressure impulse, I_P (b): dynamic pressure impulse, I_{Pd} and (c): normalized overpressure \mathcal{P} , for different M_s at P_1 ($- M_s = 1.6$, $- M_s = 2.0$, $- M_s = 2.5$, $- M_s = 3.5$, $- M_s = 4.5$).

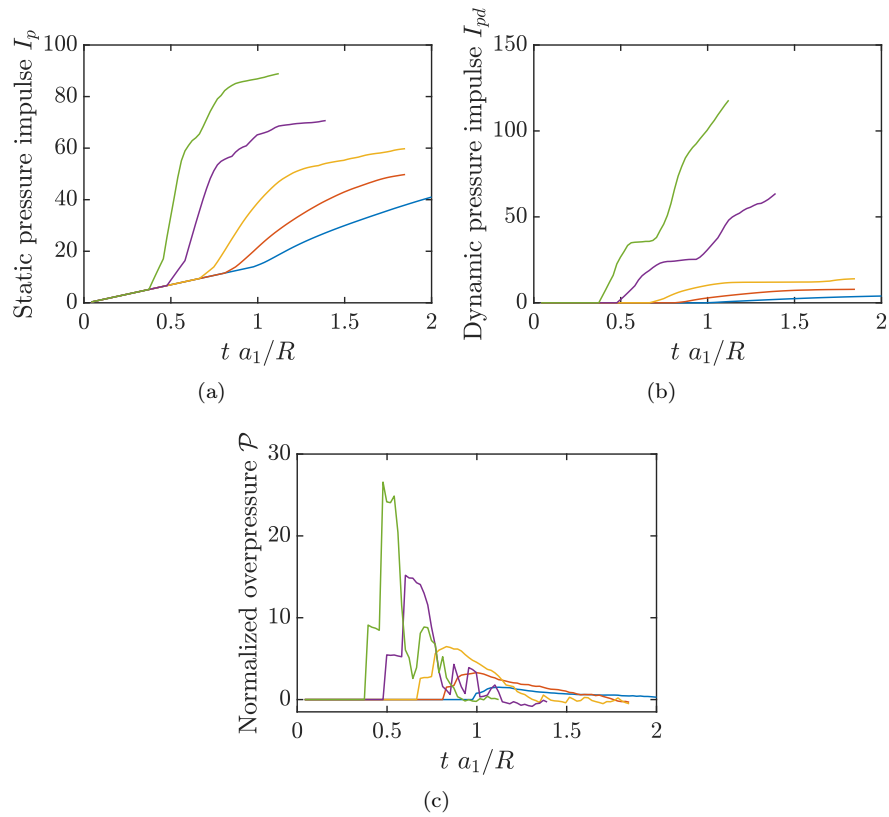


Figure 12: Time history of (a): static pressure impulse, I_P (b): dynamic pressure impulse, I_{Pd} and (c): normalized overpressure \mathcal{P} , for different M_s at P_2 ($- M_s = 1.6$, $- M_s = 2.0$, $- M_s = 2.5$, $- M_s = 3.5$, $- M_s = 4.5$).

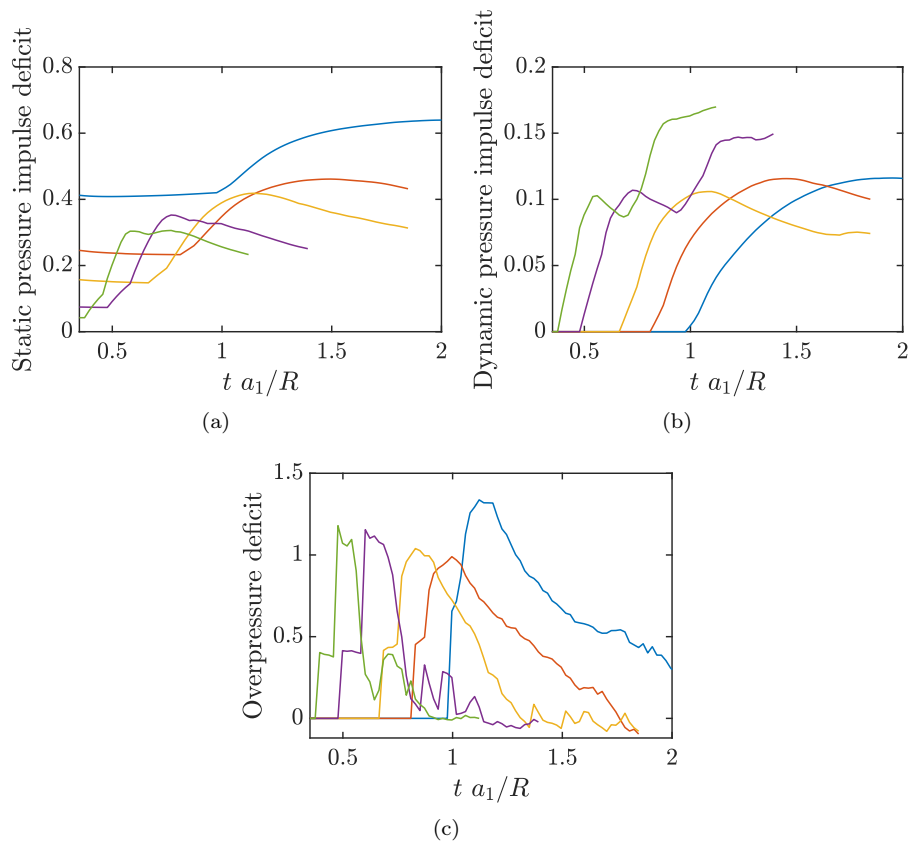


Figure 13: Time history of (a): static pressure impulse deficit (b): dynamic pressure impulse deficit and (c): overpressure deficit, for different M_s at P_2 ($- M_s = 1.6$, $- M_s = 2.0$, $- M_s = 2.5$, $- M_s = 3.5$, $- M_s = 4.5$).

289 5. Accumulation of numerical errors

290 Estimating accuracy and errors accumulation is necessary in CFD, especially
291 when dealing with high-fidelity numerical simulations. Depending on the spatial
292 resolution and on the numerical scheme, a definite error occurs due to numerical
293 integration at each time step [21]. According to Smirnov *et al.* [21], the relative
294 integration error for one-dimensional problem is:

$$S_1 = \left(\frac{h}{L_1} \right)^{k+1} \quad (13)$$

295 where h is the cell size, L_1 is the domain length and k the order of accuracy
296 of the numerical scheme. For multi-dimensional problem, the integration errors
297 can be summed up as:

$$S_{err} = \sum_{i=1}^3 S_i \quad (14)$$

298 The maximal allowable number of time steps for solving a given problem could
299 be determined by the following formula:

$$\eta_{max} = (S^{max}/S_{err})^2 \quad (15)$$

300 where S^{max} is the allowable value of the total error, which is presumed to
301 be between 1% and 5%. Smirnov *et al.* [21] have introduced another impor-
302 tant measurement of numerical errors suitable for high-performance computing,
303 which is the ratio of the maximal allowable number of time steps η_{max} to the
304 actual number of time steps used to obtain the results η :

$$R_s = \eta_{max}/\eta \quad (16)$$

305 According to Smirnov *et al.* [21], the parameter R_s can characterize the relia-
306 bility of the numerical results, i.e. how far below the limit, the simulations were
307 finalized. Indirectly, this parameter characterizes the accumulated error. The
308 higher is the value of R_s , the lower is the error. On tending R_s to unity, the

309 error tends to a maximal allowable value.

310 Table 3 summarizes the results of different grid resolutions and physical time
 311 in our simulations. As it can be seen, a quite high level of reliability is achieved
 312 in our case.

Allowable error (%)	Grid resolution	Physical time simulated (μs)	Number of time steps	Accumulated error	Allowable number of time steps	Reliability $R_s = \eta_{max}/\eta$
5	1793×1025	294	4311	9.48×10^{-16}	2.78×10^{27}	6.45×10^{23}
5	2817×1793	294	7854	5.84×10^{-17}	7.33×10^{29}	9.33×10^{25}
5	3841×2305	294	10307	1.8×10^{-17}	7.71×10^{30}	7.48×10^{26}
5	5633×3073	294	14061	6.94×10^{-18}	5.19×10^{31}	3.69×10^{27}
5	7681×3585	294	18728	7.14×10^{-19}	4.87×10^{33}	2.61×10^{29}

Table 3: Error estimates.

313 6. Conclusions

314 In this paper, shock-wave diffraction over double cylindrical wedges have
 315 been numerically investigated by means of two-dimensional high-fidelity numer-
 316 ical simulation. The objective was to study the flow structure and the vorticity
 317 formation with regards to the incident-shock-wave Mach number. Different grid
 318 resolutions were used in order to investigate the mesh sensitivity of the results.
 319 It was found that although the upstream flow topology (shape of the eddies)
 320 changes with the grid resolution, the vorticity production and the shock diffrac-
 321 tion process are quite independent from the grid resolution. In terms of rate
 322 of vorticity production and circulation, it is shown that the shock strength en-
 323 hances the vorticity production and the rate of vorticity production increases
 324 as the incident shock strength increases and remains virtually constant after
 325 an elapsed time. For the vorticity transport equation, it was found that the
 326 stretching of vorticity due to flow compressibility plays an important role in the
 327 vorticity dynamics, for low-Mach numbers regimes ($Ms \leq 2.5$). The diffusion of
 328 the vorticity due to the viscous effects is seen to be quite important compared
 329 to the baroclinic term, while this trends is inverted for higher Mach numbers

330 regimes ($M_s \geq 3.5$). In terms of shock strength, it was found that the effect of
331 the first concave surface is effective in decreasing sufficiently the dynamic pres-
332 sure impulse (up to 90 % for $M_s = 2.5$) as well as the static pressure impulse
333 (up to 75 % for $M_s = 4.5$). However for the overpressure deficit, the peaks are
334 accentuated by the passage of the reflected shock and the formation of shocklets
335 that tend to reduce the overall overpressure deficit.

336 7. Acknowledgments

337 The first author gratefully acknowledges support from the Algerian Govern-
338 ment through a Ph.D Fellowship. Computational facilities from ‘Centre Ré-
339 gional Informatique et d’Applications Numériques de Normandie (CRIANN)’,
340 Rouen, France under allocation 1998022, are acknowledged.

341 References

- 342 [1] B. Skews, The perturbed region behind a diffracting shock wave, *Journal*
343 *of Fluid Mechanics* 29 (04) (1967) 705.
- 344 [2] L. Howard, D. Matthews, On the Vortices Produced in Shock Diffraction,
345 *Journal of Applied Physics* 27 (3).
- 346 [3] T. V. Bazhenova, L. G. Gvosdeva, Y. V. Zhilin, Change in the shape of
347 the diffracting shock wave at a convex corner, *Acta Astronautica* 6 (1951)
348 (1979) 401–412.
- 349 [4] F. Gnani, K. H. Lo, H. Zare-Behtash, K. Kontis, Experimental investigation
350 on shock wave diffraction over sharp and curved splitters, *Acta Astronau-*
351 *tica* 99 (1) (2014) 143–152.
- 352 [5] M. Sun, K. Takayama, Vorticity production in shock diffraction, *Journal*
353 *of Fluid Mechanics* 478 (2003) 237–256.
- 354 [6] T. Tseng, R. Yang, Numerical Simulation of Vorticity Production in Shock
355 Diffraction, *AIAA Journal* 44 (5) (2006) 1040–1047.

- 356 [7] A. Chaudhuri, G. B. Jacobs, Dynamics of shock wave diffraction over sharp
357 splitter geometry using entropy-based artificial viscosity method, *Shock*
358 *Waves* (2017) 1–15.
- 359 [8] M. Sun, K. Takayama, The formation of a secondary shock wave behind
360 a shock wave diffracting at a convex corner, *Shock Waves* 7 (5) (1997)
361 287–295.
- 362 [9] M. K. Quinn, K. Kontis, A Combined Study on Shock Diffraction, 5th
363 Symposium on Integrating CFD and Experiments in Aerodynamics (2012)
364 3–5.
- 365 [10] J. Cai, J. Zhou, S. Liu, Z. Lin, Effects of dynamic backpressure on shock
366 train motions in straight isolator, *Acta Astronautica* 141 (2017) 237–247.
- 367 [11] J. Reeves, B. Skews, Unsteady three-dimensional compressible vortex flows
368 generated during shock wave diffraction, *Shock Waves* 22 (2) (2012) 161–
369 172.
- 370 [12] G. Abate, W. Shyy, Dynamic structure of confined shocks undergoing sud-
371 den expansion, *Progress in Aerospace Sciences* 38 (1) (2002) 23–42.
- 372 [13] J. Zhao, R. Li, H. Wu, Investigate the shock focusing under a single vor-
373 tex disturbance using 2D Saint-Venant equations with a shock-capturing
374 scheme, *Acta Astronautica* 143 (2018) 337–352.
- 375 [14] A. Chaudhuri, A. Hadjadj, O. Sadot, E. Glazer, Computational study of
376 shock-wave interaction with solid obstacles using immersed boundary meth-
377 ods, *International Journal for Numerical Methods in Engineering* 8 (89)
378 (2012) 975–990.
- 379 [15] V. Soni, A. Hadjadj, A. Chaudhuri, G. Ben-Dor, Shock-wave reflections
380 over double-concave cylindrical reflectors, *Journal of Fluid Mechanics* 813
381 (2017) 70–84.

- 382 [16] V. Soni, A. Hadjadj, O. Roussel, On the use of adaptive multiresolution
383 method with time-varying tolerance for compressible fluid flows, *Shock*
384 *Waves* (2017) 1–14.
- 385 [17] V. Soni, A. Hadjadj, O. Roussel, G. Moebs, Parallel multi-core and multi-
386 processor methods on point-value multiresolution algorithms for hyperbolic
387 conservation laws, *J. Parallel Distrib. Comput.* 123 (2019) 192–203.
- 388 [18] A. Chaudhuri, A. Hadjadj, A. Chinnayya, On the use of immersed bound-
389 ary methods for shock/obstacle interactions, *Journal of Computational*
390 *Physics* 230 (5) (2011) 1731–1748.
- 391 [19] A. Chaudhuri, A. Hadjadj, A. Chinnayya, S. Palerm, Numerical study of
392 compressible mixing layers using high-order WENO schemes, *Journal of*
393 *Scientific Computing* 47 (2) (2011) 170–197.
- 394 [20] N. Brahmi, A. Hadjadj, V. Soni, A. Chaudhuri, Analysis of shock-wave
395 diffraction over double concave cylindrical wedges. Part I: Shock dynamics,
396 *Acta Astronautica*, <https://doi.org/10.1016/j.actaastro.2020.01.025>.
- 397 [21] N. N. Smirnov, V. B. Betelin, V. F. Nikitin, L. I. Stamov, D. I. Altoukhov,
398 Accumulation of errors in numerical simulations of chemically reacting gas
399 dynamics, *Acta Astronautica* 117 (2015) 338–355.